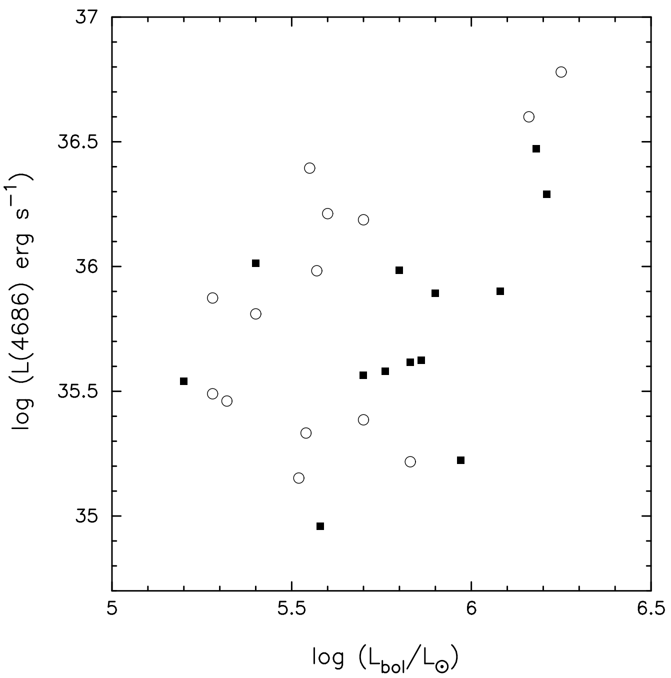

Fig. A1.— Luminosity in the He II 4686 line vs. the bolometric luminosity for WNL stars, from the measurements and analysis by Crowther & Dessart (1997). Open circles denote LMC stars; filled squares are Galactic stars. Note the huge variation in line luminosity across the WNL subclass.

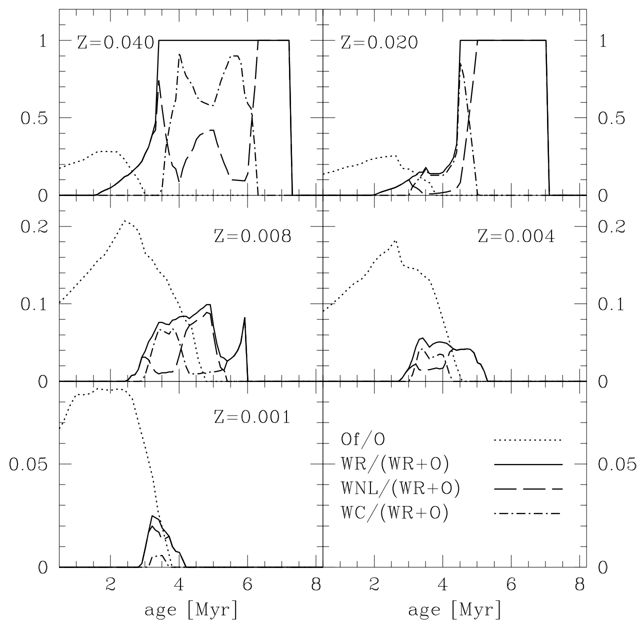

Fig. A2.— Predicted Of/O and WR/O star number ratios as a function of age for all metallicities. All models are calculated for an instantaneous burst with a Salpeter IMF. Shown are the total WR/(WR+O) (solid), the WNL(WR+O) (dashed), the WC/(WR+O) (dashed-dotted), and the Of/O number ratios. Note the change of the ordinate between the top, middle, and lower panels.

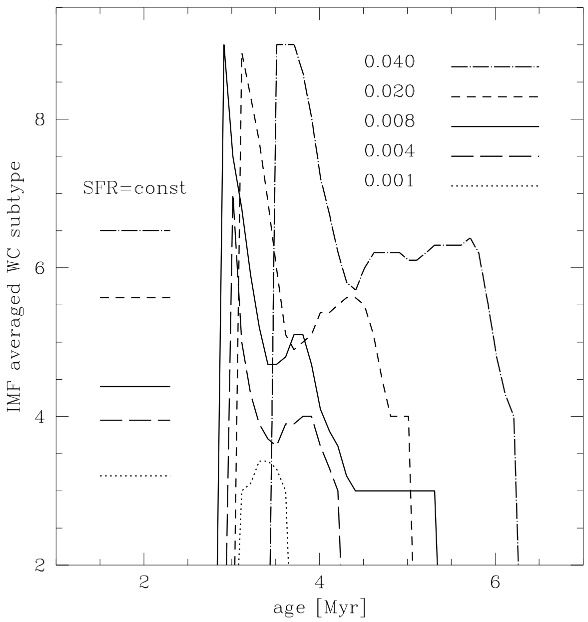

Fig. A3.— Temporal evolution of the IMF-averaged WC subtype for all metallicities (Z=0.040: dashed-dotted, 0.020: short dashed, 0.008: solid, 0.004: long dashed, 0.001: dotted). WO stars are designated by a WC3 subtype

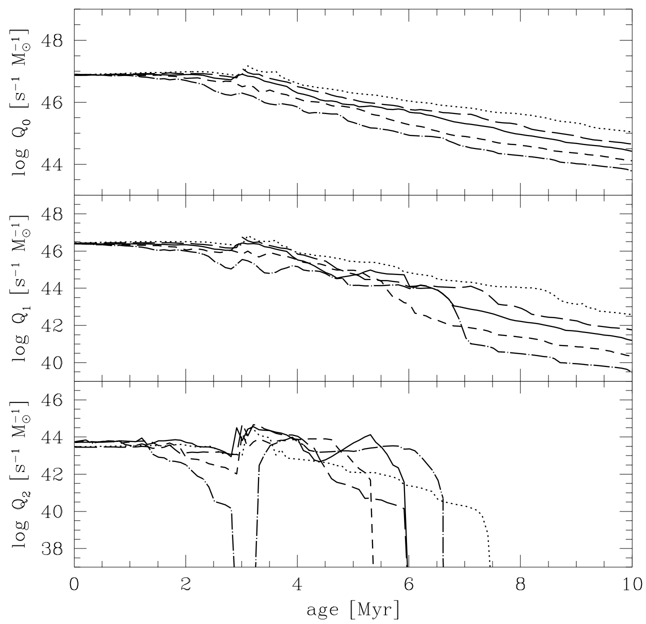

Fig. A4.— Temporal evolution of the ionizing photon flux of a stellar population (normalised to a total mass of 1 $M_\odot$) for all metallicities. *Top panel:* Lyman continuum flux, *Middle:* Flux in the He I continuum, *Lower panel:* flux in the He II continuum. Same symbols as in Fig. A3

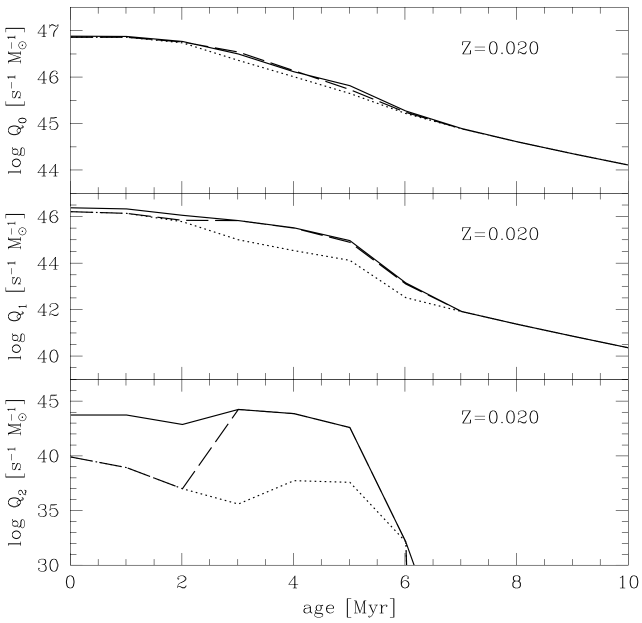

Fig. A5.— Comparison of predicted ionizing fluxes using different atmosphere models. Shown is the standard model for Z=0.020. Dotted: using plane parallel, LTE, line blanketed models of Kurucz (1992) only; Dashed: same as dotted but using spherically expanding non–LTE models for WR stars (Schmutz, Leitherer & Gruenwald, 1992); Solid: same as dashed but using spherically expanding, line blanketed, non–LTE *CoStar* models for O stars. The top, middle, and bottom panel show Q_0, Q_1,and Q_2 respectively

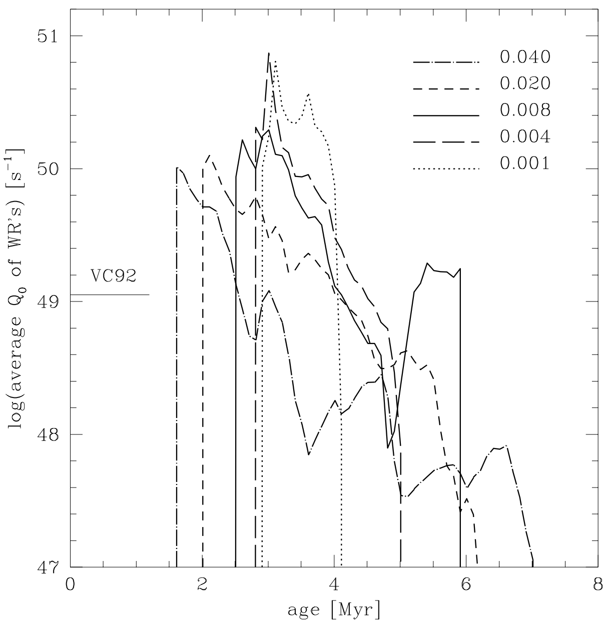

Fig. A6.— Time evolution of the average Lyman continuum luminosity provided per WR star in instantaneous burst models. The thin solid horizontal line indicates the value of $Q_O^{\rm WNL}$ from Vacca & Conti (1992). Same symbols as in Fig. A3

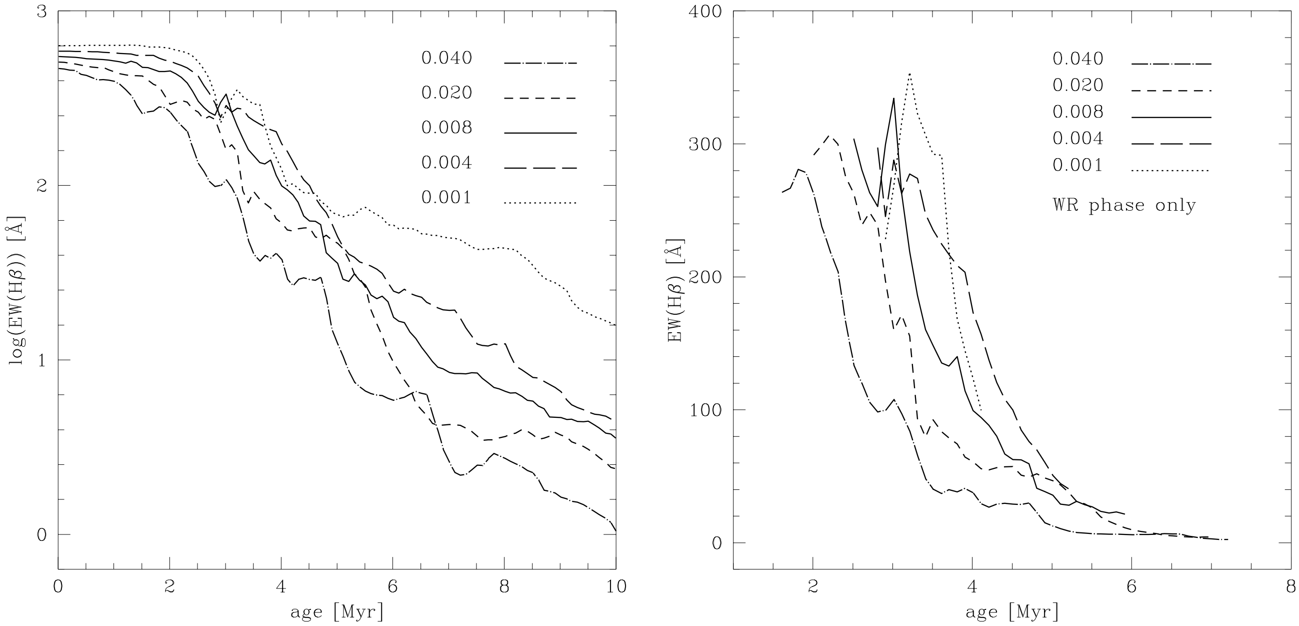

Fig. A7.— Time evolution of the Hβ equivalent width for an instantaneous burst at the given metallicity. Same symbols as in Fig. A3. *Left panel:* Logarithm of $W(\mathrm{H}\beta)$ for ages from 0 to 10 Myr. *Right panel:* Evolution of $W(\mathrm{H}\beta)$ during the WR rich phases of the burst. Horizontal lines on the margins show the maximum/minimum $W(\mathrm{H}\beta)$ during the WR phase

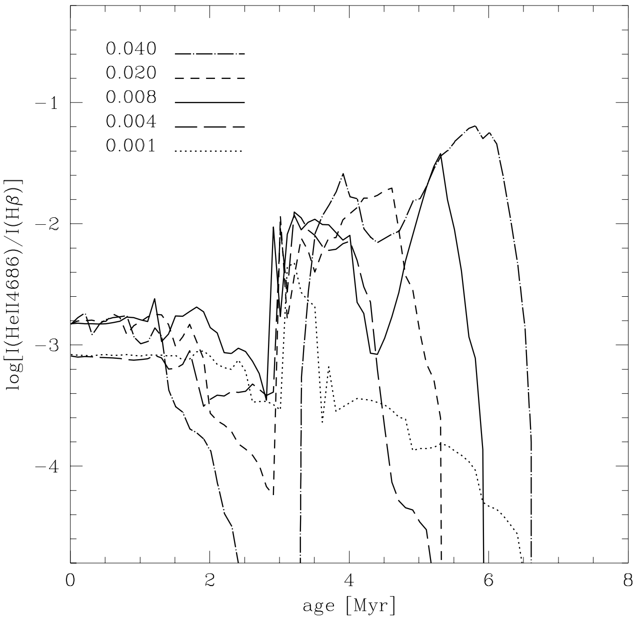

Fig. A8.— Predicted *nebular* emission line ratio of He II $\lambda4686/\mathrm{H}\beta$ as a function of age. Same symbols as in Fig. A3. See Figs. A13 and A16 for the total WR and nebular 4686 emission

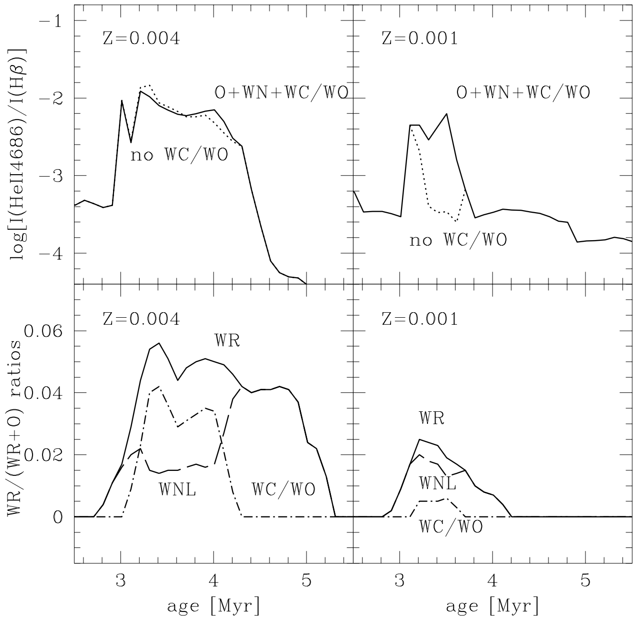

Fig. A9.— *Lower panels:* total WR/(WR+O) (solid lines), WNL/(WR+O) (dashed), and WC/(WR+O) (dashed-dotted) number ratios as a function of time for Z=0.004 (left) and Z=0.001 (right). *Upper panels:* Nebular He II $\lambda4686/\mathrm{H}\beta$ as a function of age for Z=0.004 (left) and Z=0.001 (right). The dotted lines show the predicted He II $\lambda4686/\mathrm{H}\beta$ when WC stars are excluded. This shows that both WC and (hot) WN stars contribute to the nebular He II emission

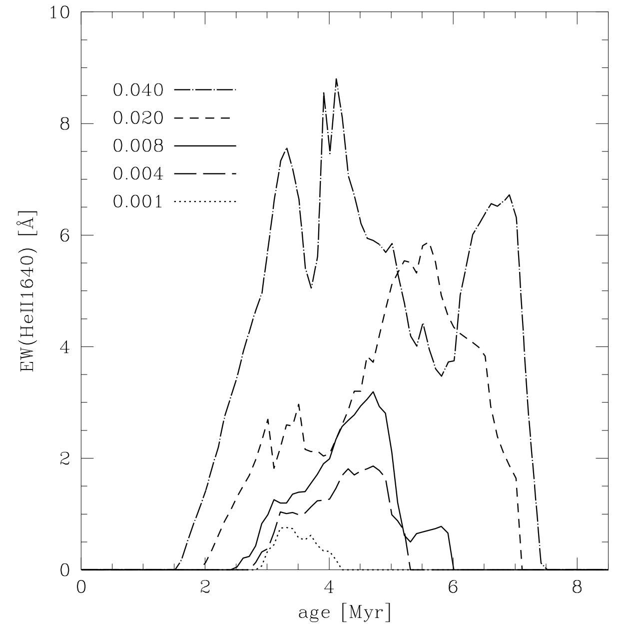

Fig. A10.— Evolution of the He II $\lambda1640$ equivalent width. Same symbols as in Fig. A3

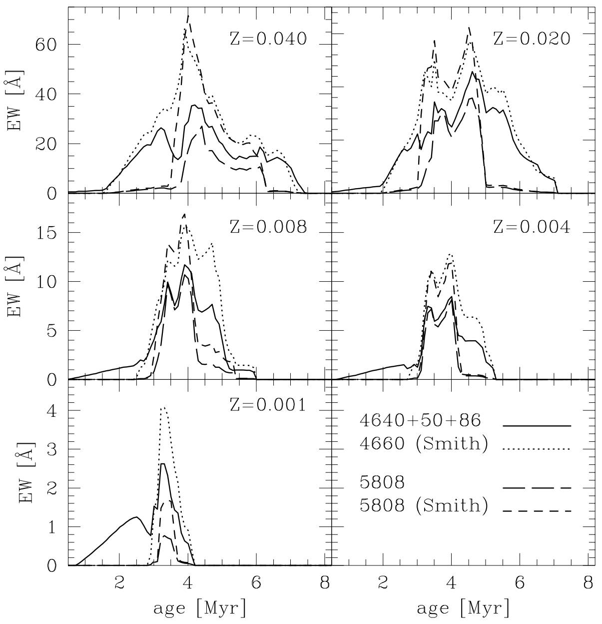

Fig. A11.— Evolution of WR bump equivalent widths for all metallicities. Solid lines: 4660 bump including N III/V $\lambda4640$, C III/IV $\lambda4650$, and He II $\lambda4686$. Long-dashed: C IV $\lambda5808$. Both following the prescriptions in Tables 1 and 2. Dotted and short-dashed lines show the WR bump equivalent widths using the prescriptions of Smith (1991; cf. Table 3)

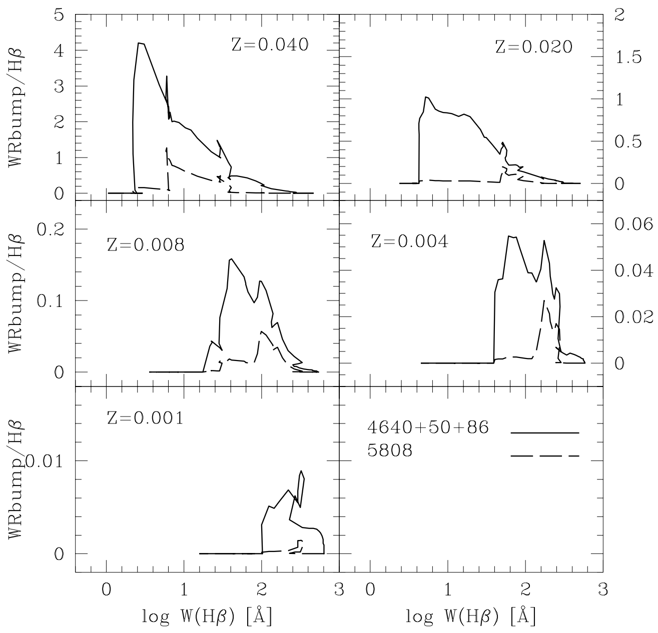

Fig. A12.— Evolution of WR bump intensities relative to Hβ for all metallicities. Solid: 4660 bump, long-dashed: C IV λ5808, computed as in Fig. A11. The less accurate values using the prescription of Smith (1991) is not shown here. Certain cases show non-uniqueness of line intensities when plotted against $W(\mathrm{H}\beta)$ (e.g. for Z=0.001, but cf. also other Figs.). This behaviour is due to the slight increase of the Hβ with time at the beginning of the WR phase (see Fig. A7), which is in turn related to the contribution of WR stars to the Lyman continuum flux

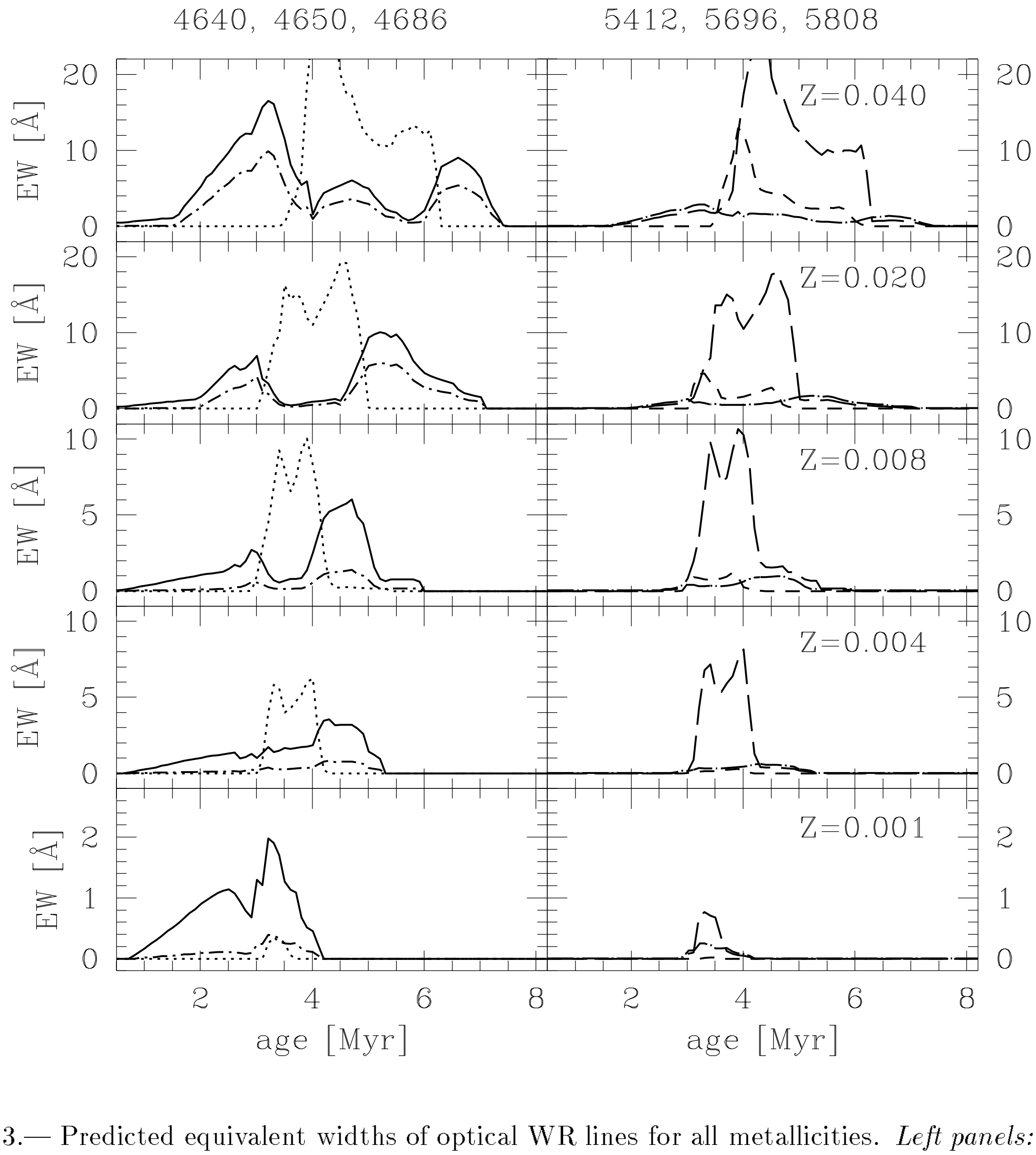

Fig. A13.— Predicted equivalent widths of optical WR lines for all metallicities. *Left panels:* He IIλ4686 (solid), C III/IV λ4650 (dotted), N III/V λ4640 (short dashed-dotted). *Right panels:* C IV λ5808 (long dashed), C III λ5696 (short dashed), He IIλ5412 (long dashed-dotted)

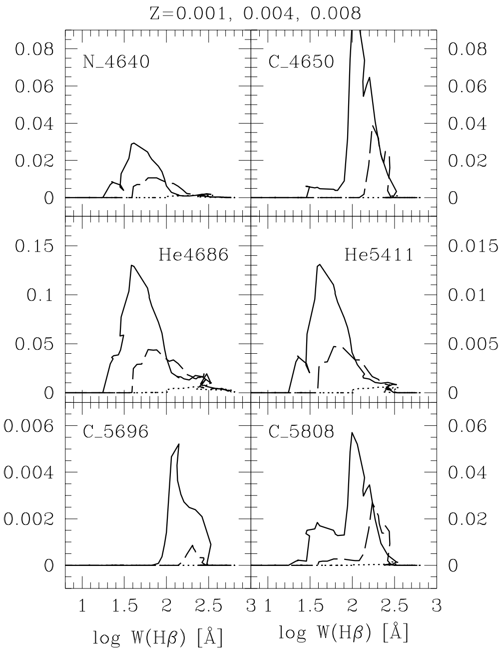

Fig. A14.— Predicted intensity ratio $I(\lambda)/I(\mathrm{H}_\beta)$ for WR lines at Z=0.008 (solid), 0.004 (long-dashed), and 0.001 (dotted)

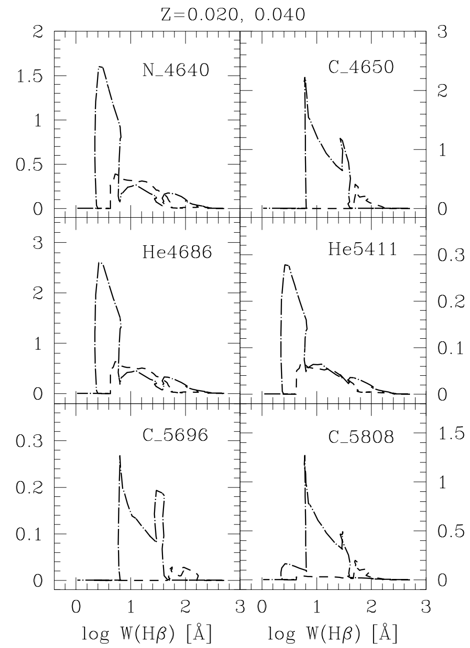

Fig. A15.— Same as Fig. A14 for Z=0.02 (short-dashed) and 0.04 (dashed-dotted)

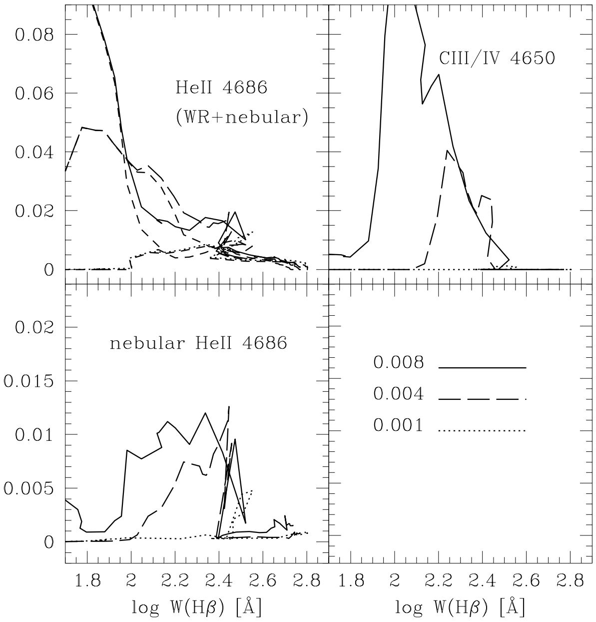

Fig. A16.— Predicted intensity ratios $I(\lambda)/I(H_\beta)$ for nebular and WR lines at $\lambda \sim$ 4650-4700 Å for Z=0.008 (solid), 0.004 (long-dashed), and 0.001 (dotted)

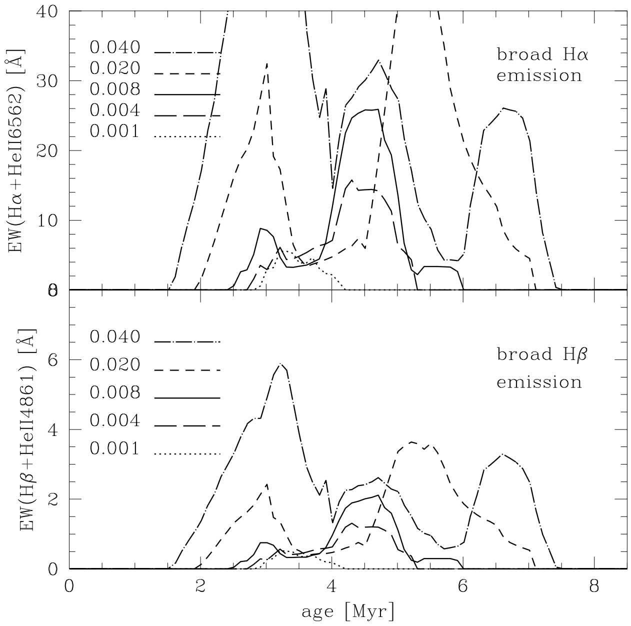

Fig. A17.— Predicted equivalent widths of Hα (upper panel) and Hβ (lower panel) blends for all metallicities. Symbols as in Fig. A3

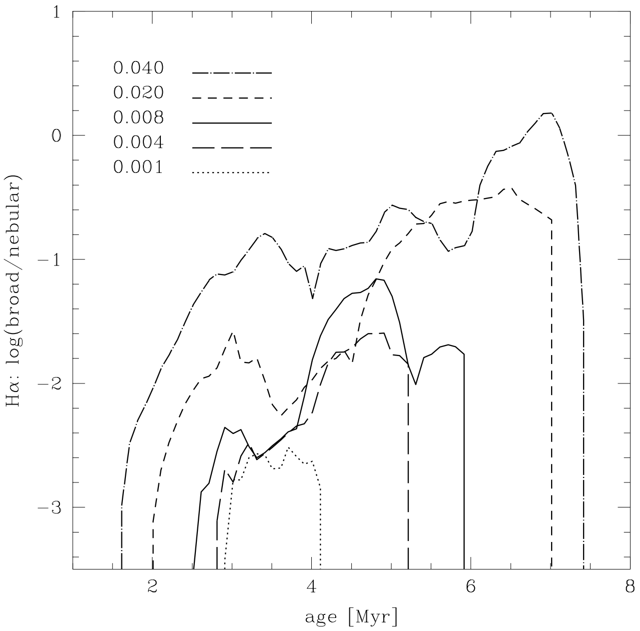

Fig. A18.— Ratio of broad WR emission to nebular Hα line for all metallicities. Symbols as in Fig. A3. The relative contribution to Hβ is nearly identical to the Hα contribution (see § 6.2.4)

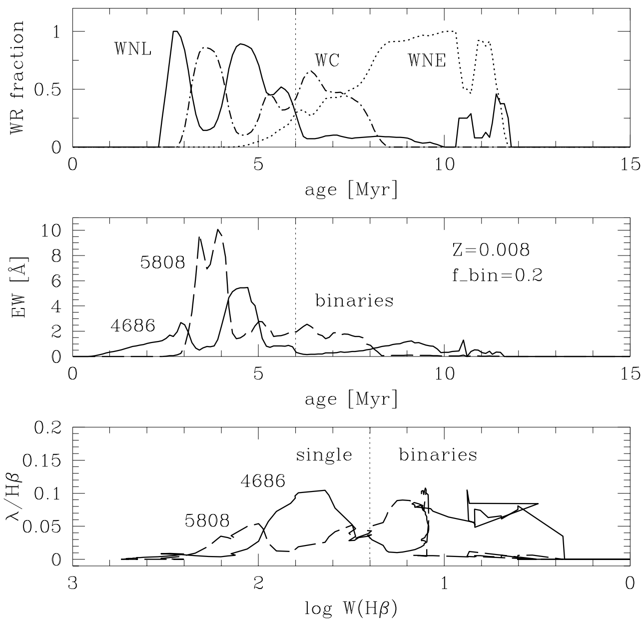

Fig. A19.— Model predictions including massive close binary stars with a binary fraction $f = 0.2$ for Z=0.008 (instantaneous burst). *Top panel:* Relative fraction of WR stars of different subtypes. *Middle:* Temporal evolution of predicted equivalent widths for He II λ4686 (solid) and C IV λ5808 (long-dashed). The arrow indicates the beginning of the phase where WR stars are predominantly formed through the binary channel. *Lower panel:* Line ratios λ/Hβ as a function W(Hβ). Same symbols as middle panel. The vertical dotted lines illustrates the clear separation of the "single star" and "binary" phases in this diagram

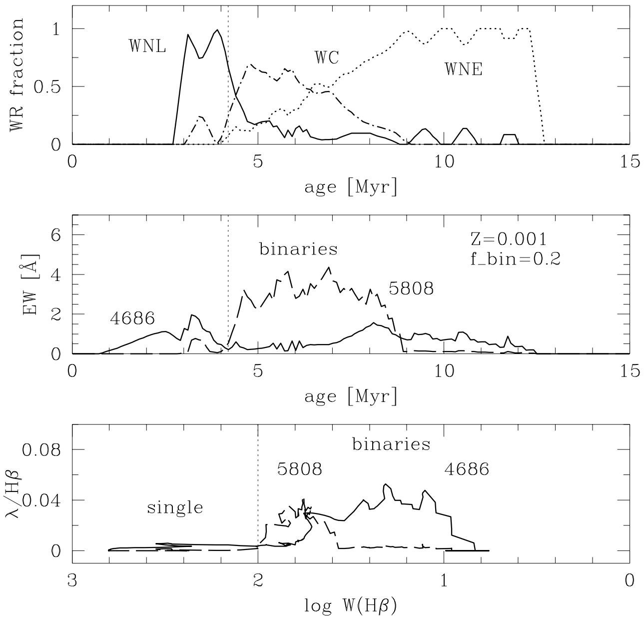

Fig. A20.— Same as A19 for Z=0.001

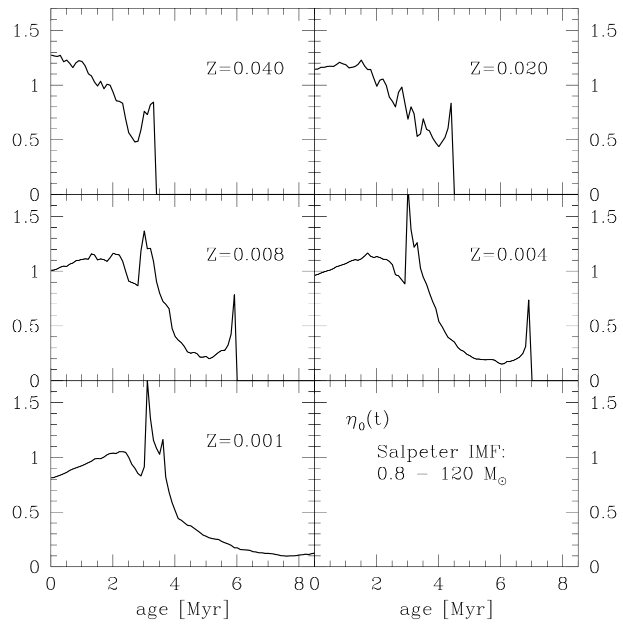

Fig. A21.— Evolution of $\eta_0(t)$ (defined by Eq. 12) in standard burst models for metallicities from Z=0.040 to 0.001

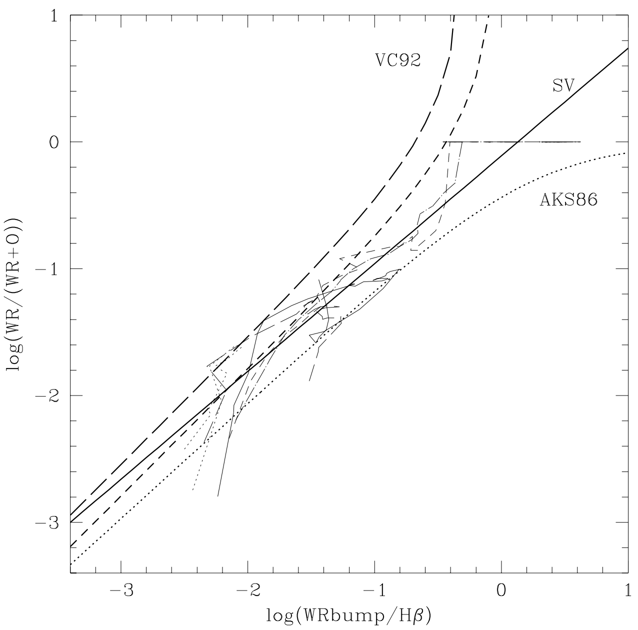

Fig. A22.— Number ratio WR/(WR+O) as a function of the intensity ratio of the WR-bump over Hβ obtained from instantaneous burst models at all metallicities (thin lines using same symbols as in Fig. A3). The thick solid line (SV) shows the fit to our models (cf. Eq. 17). Thick dashed: relation from Arnault, Kunth & Schild. Thick long-dashed: relation from VC92 (their Eq. 15 assuming $\eta = 1.$). Thick short-dashed: same as long-dashed but assuming a larger average line luminosity of log(4650-4686)=36.7

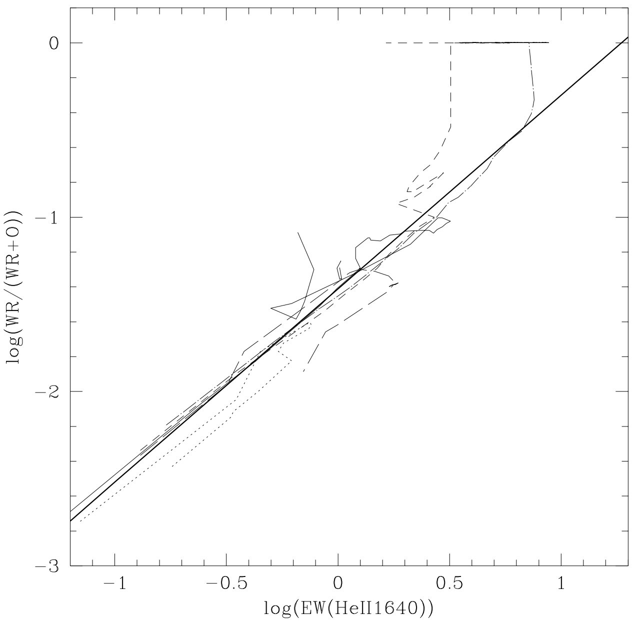

Fig. A23.— Number ratio WR/(WR+O) as a function of the He II λ1640 equivalent width (emission, in Å) obtained from instantaneous burst models at all metallicities (thin lines using same symbols as in Fig. A3). The thick solid line shows the fit to our models (cf. Eq. 18)